



ALMA MATER STUDIORUM  
UNIVERSITÀ DI BOLOGNA

ARCHIVIO ISTITUZIONALE  
DELLA RICERCA

## Alma Mater Studiorum Università di Bologna Archivio istituzionale della ricerca

Deep learning for enhancing wavefield image quality in fast non-contact inspections

This is the final peer-reviewed author's accepted manuscript (postprint) of the following publication:

*Published Version:*

Keshmiri Esfandabadi Y., Bilodeau M., Masson P., De Marchi L. (2020). Deep learning for enhancing wavefield image quality in fast non-contact inspections. STRUCTURAL HEALTH MONITORING, 19(4), 1003-1016 [10.1177/1475921719873112].

*Availability:*

This version is available at: <https://hdl.handle.net/11585/712954> since: 2020-11-02

*Published:*

DOI: <http://doi.org/10.1177/1475921719873112>

*Terms of use:*

Some rights reserved. The terms and conditions for the reuse of this version of the manuscript are specified in the publishing policy. For all terms of use and more information see the publisher's website.

This item was downloaded from IRIS Università di Bologna (<https://cris.unibo.it/>).  
When citing, please refer to the published version.

(Article begins on next page)

# Deep learning for enhancing wavefield image quality in fast non-contact inspections

Journal Title  
XX(X):1-12  
©The Author(s) 2019  
Reprints and permission:  
sagepub.co.uk/journalsPermissions.nav  
DOI: 10.1177/ToBeAssigned  
www.sagepub.com/

SAGE

Yasamin Keshmiri Esfandabadi<sup>1</sup>, Maxime Bilodeau<sup>2</sup>, Patrice Masson<sup>2</sup> and Luca De Marchi<sup>1</sup>

## Abstract

Ultrasonic wavefield imaging with a non-contact technology can provide detailed information about the health status of an inspected structure. However, high spatial resolution, often necessary for accurate damage quantification, typically demands a long scanning time. In this work, we investigate a novel methodology to acquire high resolution wavefields with a reduced number of measurement points to minimize the acquisition time. Such methodology is based on the combination of compressive sensing and convolutional neural networks to recover high spatial frequency information from low resolution images. A dataset was built from 652 wavefield images acquired with a laser Doppler vibrometer describing guided ultrasonic wave propagation in 8 different structures, with and without various simulated defects. Out of those 652 images, 326 cases without defect and 326 cases with defect were used as a training database for the convolutional neural network. In addition, 273 wavefield images were used as a testing database to validate the proposed methodology. For quantitative evaluation, two image quality metrics were calculated and compared to those achieved with different recovery methods or by training the convolutional neural network with non-wavefield images dataset. The results demonstrate the capability of the technique for enhancing image resolution and quality, as well as similarity to the wavefield acquired on the full high resolution grid of scan points, while reducing the number of measurement points down to 10% of the number of scan points for a full grid.

## Keywords

Compressive sensing, Super-resolution, Wavefield imaging, Non-destructive testing, Structural health monitoring

## Introduction

Non-Destructive Testing (NDT) and Structural Health Monitoring (SHM) techniques recognize structural features using several sensing devices and signal processing methods<sup>1</sup>. Ultrasonic techniques, including active and passive sensing, have been widely studied and applied in the field of SHM<sup>2,3</sup>. Guided ultrasonic wave inspection methods are often adopted for the detection and the characterization of defects in plate-like structures because of their high sensitivity and long propagation range<sup>4,5</sup>. Guided ultrasonic waves detection can be either based on transducers permanently bonded to the inspected environment (in SHM) or on movable or non-contact transducers (in NDT)<sup>6</sup>. In the second case, the measurement can be performed using point-by-point scanning technologies such as scanning laser Doppler vibrometers (SLDV)<sup>7</sup>, or air-coupled moving transducers<sup>8,9</sup>.

Guided ultrasonic wavefield images provide both practical and fundamental information for diagnosis tasks, including material parameter extraction and defect detection<sup>7</sup>. Imaging quality greatly affects the subsequent image analysis and processing. In fact, structural imaging in high spatial resolution reveals accurately structural details. In other words, the amount of information that can be extracted from the wavefield is directly related to the number of points at which the wave propagation is measured, enabling accurate image diagnostic for identifying waves interaction with defects such as cracks, corrosion, and impact. In most cases, high resolution (HR) wavefield images are required to

make a proper diagnosis. However, HR measuring strategies typically involve long scanning time, further increased by the adoption of extensive waveform averaging required to improve the signal to noise ratio. Therefore, there is a recognized need in reducing the number of sampled waveforms to minimize the acquisition time while increasing the signal to noise ratio without any artifacts resulting.

The Compressive Sensing (CS) method has been investigated as a mean to tackle this problem by reconstructing wavefield images from a few sampling data, thus reducing the scanning time significantly<sup>10</sup>. To improve the reconstruction quality of the compressed sensed images, different solutions were investigated in<sup>11</sup>. However, the downsampling which allows meeting the quality requirements for wavefield reconstruction is still relatively modest (20-50% of scan points retained). Alternative approaches based on CS are those presented by Harley and co-workers<sup>12,13</sup>. Recently, they used an autoencoder neural network to learn low-dimensional representations of wave propagation<sup>14</sup>. Mesnil and Ruzzene<sup>15</sup> presented a sparse

<sup>1</sup>Department of Electrical, Electronic and Information Engineering, University of Bologna, Bologna, Italy

<sup>2</sup>GAUS, Department of Mechanical Engineering, Universit de Sherbrooke, Sherbrooke, QC, Canada

## Corresponding author:

Yasamin Keshmiri Esfandabadi, Department of Electrical, Electronic and Information Engineering, University of Bologna, Bologna, Italy.

Email: yasamin.keshmiri2@unibo.it

wavefield reconstruction and damage detection technique based on the analysis of guided wavefields by locating the nonpristine material points generating scattered wavefields. In these cases, the achieved downsampling rate is significant but the subsequent recovery is not meant to be used for HR imaging, but for the extraction of information related to wave propagation (such as dispersion curves, or anomalous reflector positions).

Therefore, high-speed and HR wavefield imaging is still an open research field. Possible strategies to further increase CS performance include model-based CS<sup>16</sup>, or novel sparsity-based methods such as gradient-based<sup>17</sup>, and operator splitting algorithms<sup>18</sup>. Although these methods are generally very efficient, it is not trivial to set their parameters to have the proper reconstruction accuracy.

Recently, Neural Networks (NN) have achieved noteworthy successes in image denoising tasks because of the strong ability to learn from data<sup>19</sup>. Some authors have evaluated the combined use of NNs and CS<sup>20,21</sup>.

The idea is to firstly recover images from compressive or low resolution (LR) samples, and then map the result into HR images by applying properly trained Super-Resolution Convolutional Neural Networks (SRCNNs)<sup>22</sup>. Such concepts have been used in a large number of computer vision problems, including image enhancement, such as denoising<sup>23</sup> and deblurring<sup>24</sup>. Learning based on super-resolution was shown to be capable of obtaining HR images without any over-smoothing, no ringing and jagged artifacts such as aliasing, blur, and halo around the edges<sup>25</sup>. The first attempt to combine CS and SRCNN in wavefield imaging was done, to the best of the authors' knowledge, in a conference paper by Park et al.<sup>26</sup>, where some first qualitative results were presented. The approach described in Park's work was based on a training set constituted by generic heterogeneous images.

In this work, we have investigated i) how crucial in the quality of the HR image recovery can be the creation of a large and representative training database of wavefield images and the proper tuning of CS parameters, and ii) the move from SRCNN to *Very-Deep Super Resolution* (VDSR) procedures. Deep neural network are NN with multiple layers between the input and output layers. Thanks to their complexity, they achieve superior performances with respect to conventional NN<sup>27</sup>.

Finally, we have quantified the benefit brought by the proposed approach with different performance metrics.

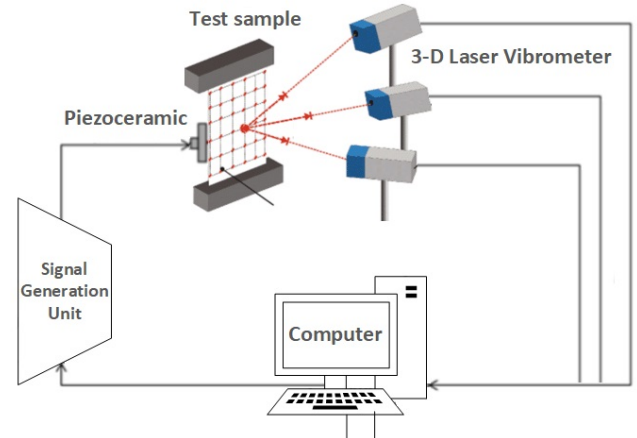
The paper is organized as follows. Section II describes the basics of CS for wavefield acquisition. Section III presents the details of the wavefield imaging HR reconstruction algorithm. Section IV illustrates the wavefield dataset that was created for training and validating the application of SRCNN and VDSR to guided ultrasonic wavefield imaging. Next, Section V presents the experimental results. Finally, Section VI summarizes the main findings of the work and provides recommendations for future investigations.

## Compressive sensing of wavefields

### Wavefield imaging basics

The term *guided ultrasonic wavefield imaging* is generally referred to the analysis of series of images representing

the time evolution of propagating guided ultrasonic waves and, possibly, their interaction with defects. The image wavefields can be generated and received with various kinds of transducers and may allow to diagnose the health of structures by determining the location and the extent of the defects<sup>28</sup>.



**Figure 1.** Experimental setup used to measure ultrasonic guided wavefields.

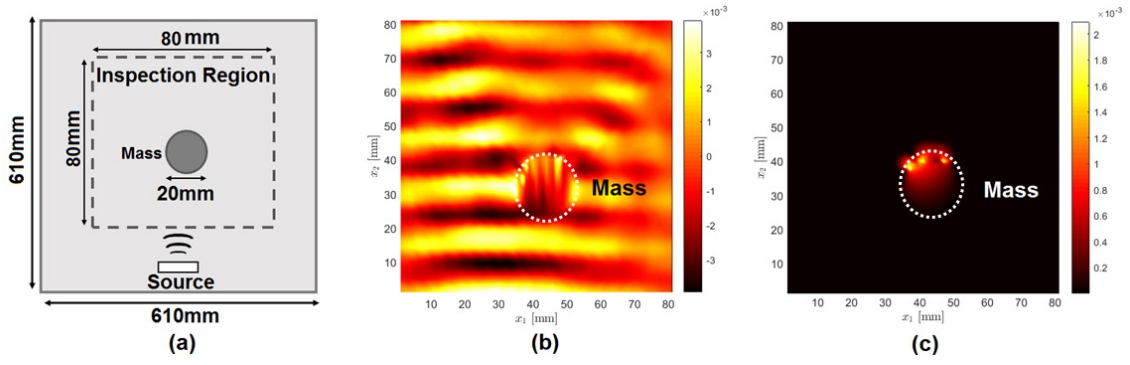
In the current work, we focus on guided ultrasonic wavefields generated by piezoelectric transducers attached to the inspected structures, and acquired with SLDV in the spatial and temporal domains. More specifically, non-contact measurement of the in-plane and out-of-plane velocity is performed using a 3-D Laser Doppler Vibrometer (3D-LDV) over a square grid of points to extract the required information. A sketch of the setup adopted for ultrasonic wavefield measurement is shown in Fig.1. Waves travel across the inspection area and are recorded at several measurement grid points.

The data is stored in 3D arrays  $W(x, y, t)$ , taking into account measurement locations and time instants. 3D data arrays contain information that can be used for structural characterization<sup>28</sup>.

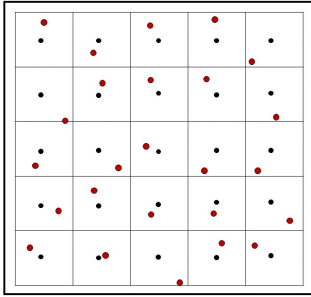
As an example of a guided ultrasonic wavefield image, Fig.2 (a) and (b) show the experimental setup and a snapshot at  $98\mu\text{s}$  of waves propagating in a simple aluminum plate and interacting with a clamped mass. The multiple wavefronts generated by the embedded transducer and scattered by discontinuities are clearly visible. In the selected frequency range (75 kHz), two modes ( $S_0$  and  $A_0$ ) are generated, but  $A_0$  mode has much greater amplitude than  $S_0$  mode.

Wavefield data can be analyzed in time and frequency domains<sup>28</sup> or by using multiscale representations<sup>30</sup>. Time slice images, waveform envelopes, accumulated kinetic energy<sup>31,32</sup>, and standing wave filtering<sup>33</sup>, are useful features to highlight the characteristics of the inspected medium and the presence of defects. For example, Fig.2 (c) shows that the processing of wavefield acquisitions can be adopted to highlight the position of the defect<sup>29,34,35</sup>.

In recent work<sup>36</sup>, an improved imaging method was developed to obtain accurate results of localization and sizing damages in metallic plates and composite laminates. Kudela et al.<sup>37</sup> studied the relation between impact energy and BVID detectability, wavenumber adaptive image filtering.



**Figure 2.** (a) Sketch of a setup constituted by a simple aluminum plate with a clamped mass, (b) Snapshot at  $t = 98 \mu s$  of the measured ultrasonic wavefield; (c) damage image generated by computing the maximum value of the wavenumber-domain filtered signal, as suggested in<sup>29</sup>. The white dot circle represents the actual position of the clamped mass.



**Figure 3.** Jittered sampling of the measurement region: the black dots represent the scan points obtained by regularly subsampling the  $x_1 - x_2$  space; their position is then randomly perturbed (red circles) to define the new scan points with coordinates  $x_{u1}$  and  $x_{u2}$ .

### Compressive sensing theory

In this work, CS is used as a mean to reconstruct wavefield images from a small number of undersampled data and accelerate the data acquisition process. The CS theory<sup>38</sup> states that, under specific conditions, a signal  $s \in R^n$  can be reconstructed from a linear combination of random measurements  $y \in R^m$ .

The measurements  $y$  can be expressed as the result of a vector-matrix product:

$$y = \Phi s \quad (1)$$

where  $\Phi \in R^{m \times n}$  is the measurement matrix, and  $m$  is the number of measurements, which can be much smaller than the dimension of the signal ( $m \ll n$ ).

In this work, we follow the mathematical notation adopted in<sup>11</sup>:  $s$  is the wavefield signal acquired (after averaging) in HR;  $n_1$ ,  $n_2$  and  $n_3$  are the number of scan points in the  $x_1$  and  $x_2$  coordinates (i.e. the spatial grid), and the number of samples in the time axis, respectively. Therefore, the dimension of the signal  $s$  sampled according to the full grid is  $n = n_1 \times n_2 \times n_3$ .

In order to reduce the number of acquisition points in space, and consequently the acquisition time,  $\Phi$  acts as a subsampling operator, more specifically, the *jitter subsampling operator* presented in<sup>39</sup> can be adopted. Such subsampling is based on the definition of an equispaced undersampled grid of scan points which are subsequently perturbed (see Fig. 3).

The signal  $s$  can be recovered from the compressed measurements  $y$ , if it has a sparse representation in some model basis  $\Psi \in R^{n \times n}$ , as following:

$$s = \Psi \alpha \quad (2)$$

Furthermore, the downsampling measurement matrix  $\Phi$  has to be incoherent with the model basis  $\Psi$ <sup>40</sup>. This means that  $\mu \sim 1$ ,  $\mu$  being the measure of the largest correlation between any two elements of  $\Phi$  and  $\Psi$ :

$$\mu(\Phi, \Psi) = \sqrt{n} \max_{1 \leq i, j \leq n} |\langle \varphi_i, \psi_j \rangle|, \quad (3)$$

where  $\varphi_i$ ,  $\psi_j$  are the rows of  $\Phi$  and the columns of  $\Psi$ , respectively, and  $\mu \in [1, \sqrt{n}]$ .

Many CS recovery algorithms have been proposed to find the coefficients  $\alpha$  and consequently recover the signal  $s$ , such as the so called Orthogonal Matching Pursuit (OMP)<sup>41</sup>, or Iterative Hard Thresholding (IHT)<sup>42</sup>, and Iterative Soft Thresholding (IST)<sup>43</sup>.

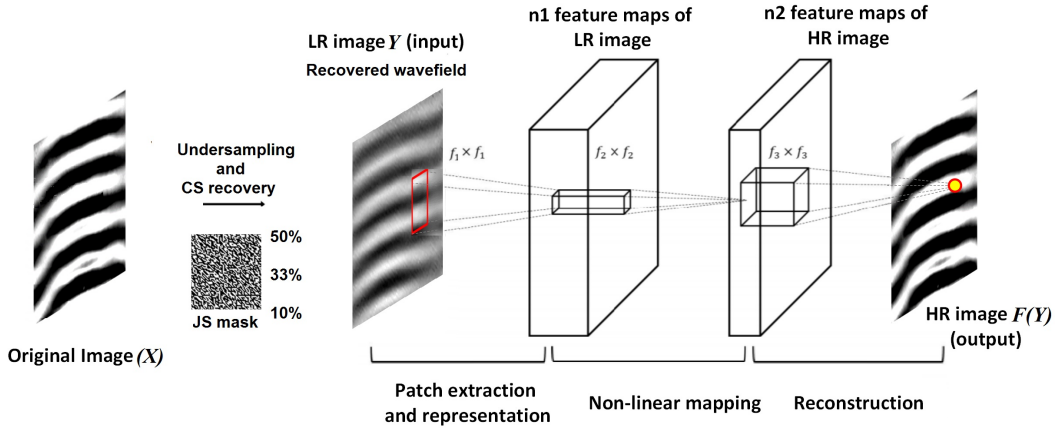
When the measurements corrupted by noise and data are not exactly sparse, the signal is still compressible, and can be recovered by solving a  $\ell_1$ -norm minimization problem (Basis Pursuit Denoising<sup>44</sup>). In this work, an  $\ell_1$ -minimizer based on the spectral projection gradient algorithm (SPGL1)<sup>45</sup> was adopted.

Three undersampling cases were considered. These three values are representative of a medium (50% of retained scan points), consistent (33%) and very consistent (10%) spatial grid undersampling. These percentages are referred to as Compression Rates (CRs) of the reconstructed wavefield.

The time waveforms associated to the retained scan points provide the input wavefield data to the CS reconstruction based on the  $\ell_1$ -minimization. Fourier (2D, 3D) exponentials have been used to generate the sparsifying model bases  $\Psi$ . Detailed analysis of these representation domains are presented in<sup>10</sup>. The following section presents how image recovery can be improved by combining the CS recovery with conventional or deep NNs.

### Single image super-resolution

Super-resolution (SR)<sup>46</sup> refers to the task of restoring HR images from LR observations, such as those resulting from compressed acquisitions. Depending on the number of input low resolution images, the SR can be divided into Single



**Figure 4.** Overview of the SRCNN scheme for HR image reconstruction.

Image Super-Resolution (SISR) and Multi-Images Super Resolution (MISR)<sup>47</sup>. SISR has typically higher efficiency than MISR<sup>48</sup>. Super-resolution algorithms can be roughly divided into: i) interpolation-based methods such as bicubic interpolation<sup>49</sup>, ii) reconstruction-based methods which are typically very efficient and fast<sup>50, 51, 52</sup>.

### Super-resolution convolutional neural network

Among learning based methods, the one based on SRCNN was the first which was applied in wavefield imaging<sup>26</sup>. In this work, we have compared the results achievable with this method with the deep learning strategies which will be introduced in the following subsection. The architecture of the SRCNN is shown in Fig. 4. As can be seen, SRCNN is a 3-layer CNN. The tasks performed by these three layers are: patch extraction and representation, non linear mapping, and reconstruction, respectively. The *patch extraction and representation* layer extracts patch from the LR input image and compute the following mapping function  $F$ :

$$F_1(\mathbf{Y}) = \max(0, W_1 * \mathbf{Y} + B_1) \quad (4)$$

where  $Y$ ,  $W_1$ ,  $B_1$ ,  $f_1$  and  $n_1$  represent the LR image, the applied filters, the biases, the filter size, and the number of filters respectively. More specifically,  $W_1$  corresponds to  $n_1$  filters, whose size is  $f_1 \times f_1$ , being  $f_1$  the spatial size of a filter. Following<sup>22</sup>. The output is thus composed of  $n_1$  feature maps, and  $B_1$  is an  $n_1$ -dimensional vector.

As can be seen in Fig. 4, in this work, the input to SRCNN is made of the wavefields recovered from the CS procedure, and acquired with different compression rates (50%, 33% and 10%). Moreover, the CS-recovered images have been cropped into a set of  $f_{sub} \times f_{sub}$ -pixel sub-images, to further expand the training set.

The middle layer involves a *non-linear mapping*, which maps the feature vectors in  $F_1$  non-linearly to another set of feature vectors ( $F_2$ ). The operation of middle layer is as follows:

$$F_2(\mathbf{Y}) = \max(0, W_2 * F_1(\mathbf{Y}) + B_2) \quad (5)$$

where  $W_2$  is an array of  $n_2$  filters whose size is  $n_1 \times f_2 \times f_2$ , and  $B_2$  is an  $n_2$ -dimensional vector.

Finally, the *reconstruction* layer generates the final HR image. The operation of the last layer is as follows:

$$F(\mathbf{Y}) = W_3 * F_2(\mathbf{Y}) + B_3 \quad (6)$$

$W_3$  has a size of  $n_2 \times f_3 \times f_3$ , and  $B_3$  is a vector. In this work,  $n_1=64$ ,  $f_1=9$ ,  $n_2=32$ ,  $f_2=5$ ,  $f_3=5$ .

The SRCNN scheme is first used in a training phase with a training dataset for estimating its parameters, and then in a validation phase, with a testing dataset. In the training phase, the network parameters  $\Theta = W_1, W_2, W_3, B_1, B_2, B_3$  are estimated. This is achieved through minimizing the error between the reconstructed images  $F(Y_i; \Theta)$  and original high resolution image  $X$ . The error function  $E$  is given by the mean squared error:

$$E(\Theta) = \frac{1}{n} \sum_{i=1}^n \|F(Y_i; \Theta) - X_i\|^2 \quad (7)$$

where  $n$  is the number of training images,  $X_i$  is a set of HR images, and  $Y_i$  is the set of their corresponding LR images<sup>22</sup>.

In the testing phase, image quality metrics are used to assess the recovery performance of the HR image for LR cases not included in the training dataset.

### Very-deep super resolution

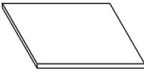
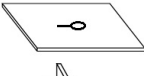

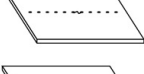

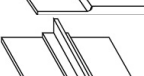


To further improve the reconstruction accuracy, a VDSR architecture was evaluated in this work. Deep structured learning<sup>53</sup> is a branch of machine learning algorithms based on directly learning diverse representations of data. Deep learning has shown superiority over conventional machine learning algorithms in computer vision<sup>19</sup> and speech recognition<sup>54</sup> tasks. Most modern deep learning models are based on NNs. Very deep models used in SISR tasks are usually referred to as VDSR models<sup>55</sup>.

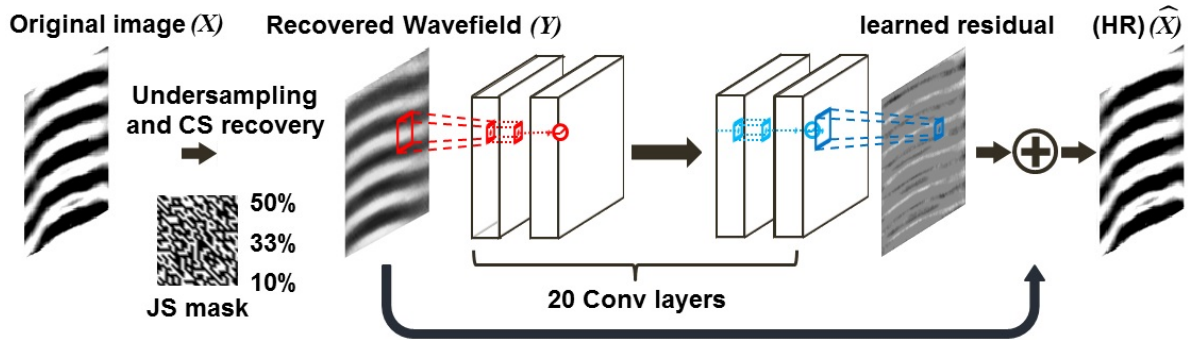
As shown in Fig. 5, the VDSR adopted in this work has 20 layers which is consequently much deeper compared with SRCNN which only had 3 layers. As suggested in<sup>56</sup>, all kernel sizes are set equal to  $3 \times 3$ . In the SRCNN, the HR image is generated directly from the learned features. In the VDSR, the neural network performs a *residual-learning*, in the sense that the output of the NN is an image which should be added to the original LR image  $Y$  to produce the estimated HR one ( $\hat{X}$ ).

Defining a residual image  $R = Y - X$ , the error function becomes:

$$E(\Theta) = \frac{1}{2} \|R - F_R(Y)\|^2 \quad (8)$$

**Table 1.** Geometrical features of the aluminum (AL) and carbon fiber reinforced polymer (CFRP) structures

Category	Features	Thickness (mm)	Size (mm)	Illustration
Aluminum plate	Simple	2 mm	610×610	
Aluminum plate	Hole and defect	3 mm	620×620	
Aluminum plate	T-spar	Species Change	610×610	
Aluminum plate	Rivet	2 mm	620×620	
CFRP plate	Simple	3 mm	500×500	
CFRP plate	Thickness variation	Taper angle	500×500	
CFRP plate	T-spar	Species Change	620×620	
CFRP plate	Curved	3 mm	510×510	

**Figure 5.** Overview of the VDSR scheme for HR image reconstruction.

where  $F_R(X)$  is the network prediction of the residual. Thus, the network is learning the residual error between the output (HR image) and input (LR image). The VDSR network used in this work takes the CS recovered images as LR input. More specifically, the original full grid training images are reconstructed by using CS technique with different CRs and using Fourier exponentials as sparsifying basis.

## Experimental validation

### Training and testing of SRCNN and VDSR

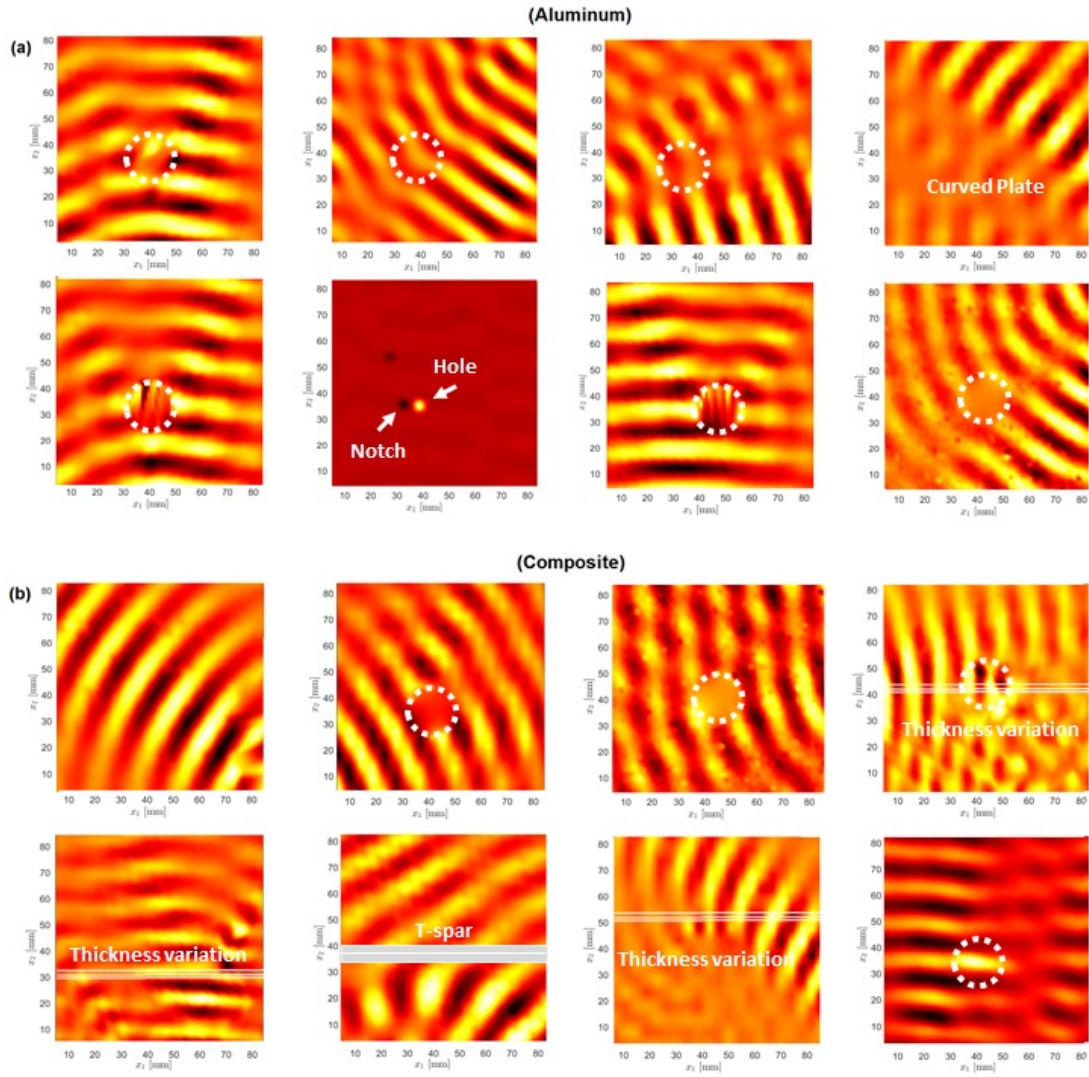
In this work, the training of the SRCNN was performed based on the open-source package *Caffe*<sup>57</sup>. Two different training datasets were considered:

- a Non-Wavefield Images or NWI dataset constituted by 652 heterogeneous images including photos of people, animals, cities and more, joining the *General-100*<sup>58</sup>, the *91-image*<sup>59</sup>, and the *ImageNet* datasets<sup>60</sup>;
- and a Wavefield Images or WI dataset, having the same cardinality as the first one, but constituted of actual

guided ultrasonic wavefield images (size equal to  $509 \times 509$  pixels.)

Our aim was to show how the type and number of training cases affect the performance of the HR image recovery.

The wavefield images were collected with a SLDV in a large number of different setups and on a dense grid of points to generate HR images. The excitation signal was a sinusoidal burst (central frequency equal to 75kHz) applied to a circular piezoelectric transducer (10 mm in diameter) and bonded on the surface of the plates. Averaging and post-processing procedures were employed to extract displacement images with high signal to noise ratios. Some sample training images are depicted in Fig. 6, while materials and geometries of the test structures are reported in Table I. As can be seen, the dataset includes both aluminum (AL) and carbon-fiber reinforced polymer (CFRP) plates, with irregularities such as thickness variations, T-spars and rivets. On the whole, the WI dataset contains 326 cases in which the presence of anomalies was simulated with magnets (20mm in diameter) and 326 cases of undamaged structures.



**Figure 6.** Examples of guided ultrasonic wavefield images related to Aluminum and CFRP plates setups which were used to train the SRCNN and VDSR. Plate features and mass positions (dotted circles) have been highlighted.

In the training phase of the SRCNN scheme, the original full wavefield images are subdivided in  $32 \times 32$  pixel sub-images. In total, 177687 sub-images were used in the training phase. The LR samples were generated from the HR ones by applying the CS recovery to subsampled versions of the original images. More specifically, the downsampling was achieved with the jittered method described in<sup>10</sup>.

Finally, we have tested the wavefield data recovery with VDSR<sup>55</sup> trained using the same wavefield images used for the SRCNN scheme. Differently from SRCNN, VDSR patch size is  $41 \times 41$  pixels, while the batch size is equal to 64. The network was then trained using the MATLAB Deep Learning Toolbox, using the same configuration parameters adopted in<sup>55</sup>. Moreover, gradient clipping was adopted to prevent gradient explosions and speed up the training.

#### Quantitative validation

To quantitatively evaluate the reconstructed super-resolution images, we have computed two types of image quality metrics: Peak signal-to-noise ratio (PSNR)<sup>61</sup> and structural similarity index (SSIM)<sup>62</sup>.

The PSNR is defined as follows:

$$PSNR(x, \hat{x}) = 10 \log \frac{Nmax}{MSE} \quad (9)$$

where  $Nmax$  is the maximum pixel value and (MSE) is Mean-Square-Error of the pixels between the original full wavefield image and its reconstruction from the LR observation. A high PSNR value means high quality recovery. Obviously, the maximization of PSNR implies the minimization of MSE as objective function.

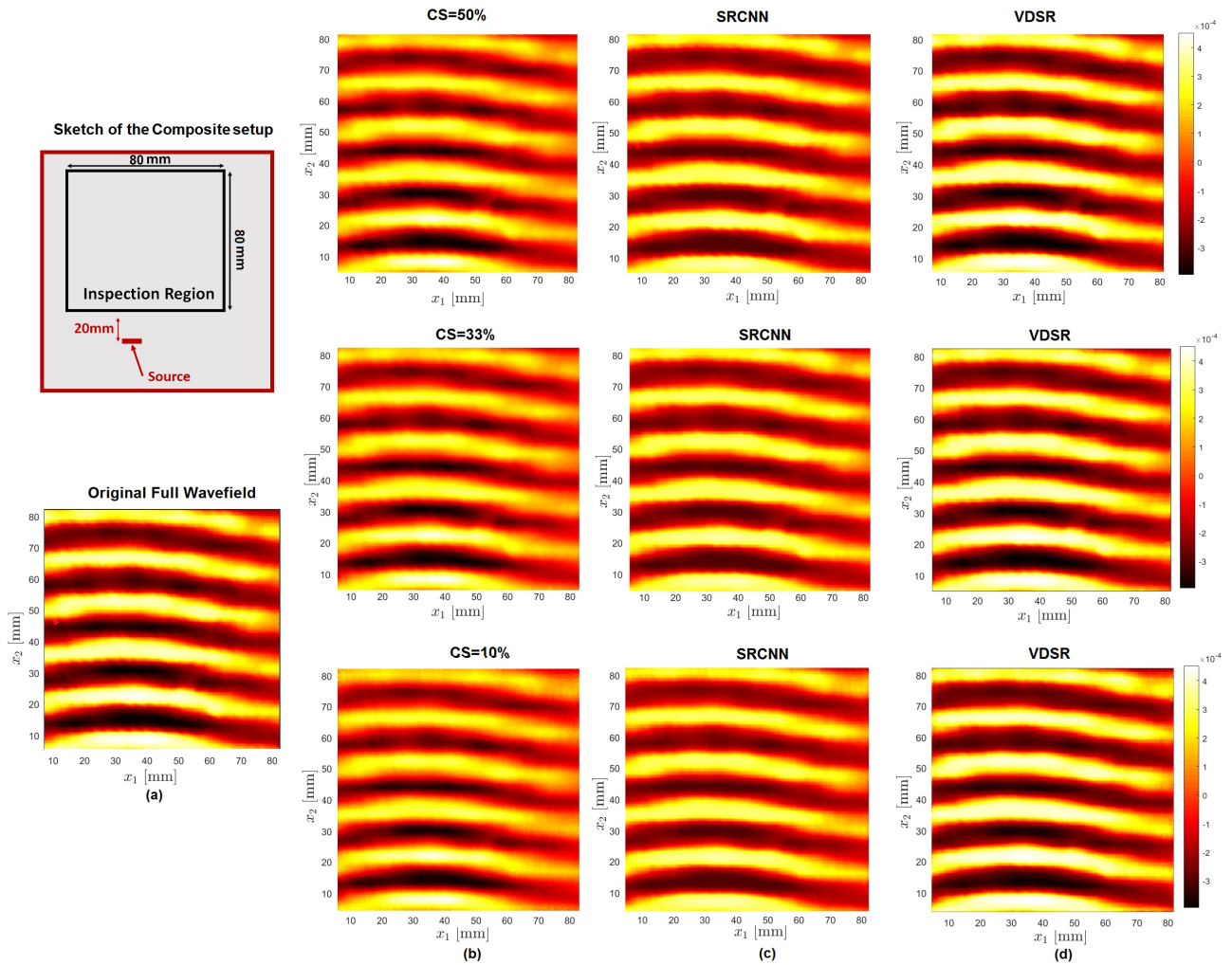
The SSIM<sup>62</sup> was used to measure the similarity between the original wavefield and the HR recovered one:

$$SSIM(x, y) = \frac{(2\mu_x\mu_y + c_1)(2\sigma_{xy} + c_2)}{(\mu_x^2 + \mu_y^2 + c_1)(\sigma_x^2 + \sigma_y^2 + c_1)} \quad (10)$$

where  $\mu_x$ ,  $\mu_y$ ,  $\sigma_x$ ,  $\sigma_y$  and  $\sigma_{xy}$  are the local means, standard deviations, and cross-covariance for images  $x$  and  $y$ .  $c_1 = (k_1L)^2$ ,  $c_2 = (k_2L)^2$ , and  $L$  are the dynamic range,  $k_1 = 0.01$ , and  $k_2 = 0.03$ .

## Results and discussion

In this section, results of the recovery of HR images by means of CS and NN are presented to assess qualitatively and



**Figure 7.** Wavefield images recovered for the simple CFRP plate using various methodologies; (a) sketch of the setup and original wavefield image; (b) images recovered uniquely with the CS procedure for CRs:50%, 33% and 10%; (c) images recovered with the CS and SRCNN; (d) images recovered with the CS and VDSR.

**Table 2.** The results of PSNR using CS and NN methods trained by Non Wavefield Images (NWI) and Wavefield Images (WI), and the results of PSNR using bicubic method trained by Wavefield Images (WI).

HR recovery	CR=50 [%]		CR=33 [%]		CR=10 [%]	
	Curved CFRP	Simple AL	Curved CFRP	Simple AL	Curved CFRP	Simple AL
CS	42.65	43.05	41.40	40.61	35.22	27.88
CS+SRCNN (NWI)	42.97	43.19	41.79	40.63	36.00	29.56
CS+SRCNN (WI)	43.96	43.45	43.42	40.65	36.83	30.22
Bicubic+VDSR (WI)	43.81	42.54	42.17	40.50	36.82	34.36
CS+VDSR (WI)	44.87	45.57	43.50	41.62	37.15	34.60

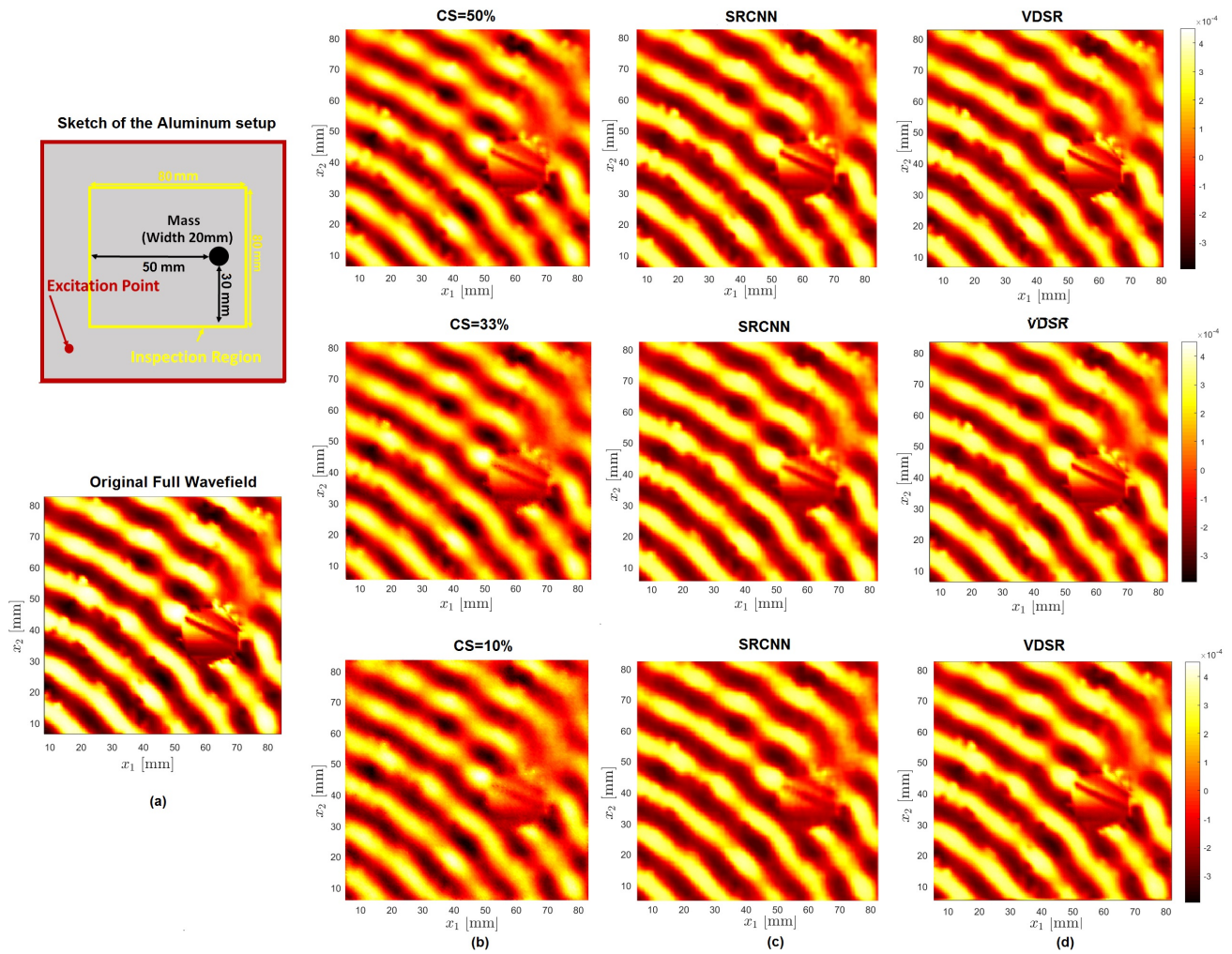
quantitatively the performance of the proposed methodology as a function of CR and NN characteristics. It must be clarified that the images used in this assessment do not belong to the training dataset. In addition, the combination of the conventional Bicubic interpolation with NN was evaluated, to quantify the advantage brought by the adoption of CS schemes.

The qualitative performance of the CS recovery combined with SRCNN and VDSR can be observed in Figs. 7 and 8 for the two specific test cases of a curved CFRP plate and an aluminum plate, respectively. In particular, it can be observed how the image recovered with the combination of CS and VDSR is very similar to the original HR wavefields

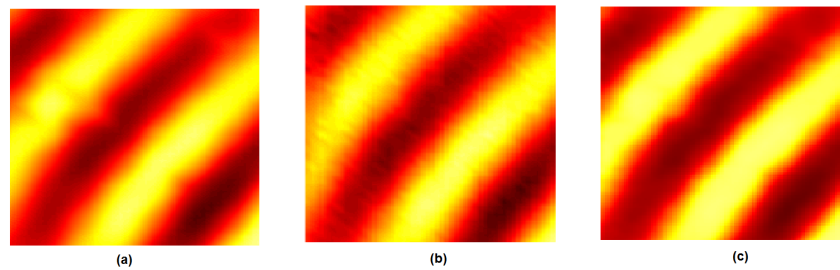
in both cases, even for very low CRs. The improvement with respect to the pure CS recovery is quite evident, especially by focusing on the details, as those shown in Figs. 9 and 10.

Figs. 11 and 12 present the comparison in terms of the SSIM achieved with the CS recovery and the training of the SRCNN and VDSR schemes with varying CRs. SSIM values are computed for the wavefield images relative to the aluminum and CFRP plates shown in Figs. 7 and 8. The results show that the value of SSIM of the recovered wavefield image trained by VDSR network is significantly higher in all the considered cases. Also clearly visible is the beneficial effect brought by the adoption of the WI dataset with respect to the results achieved by using the

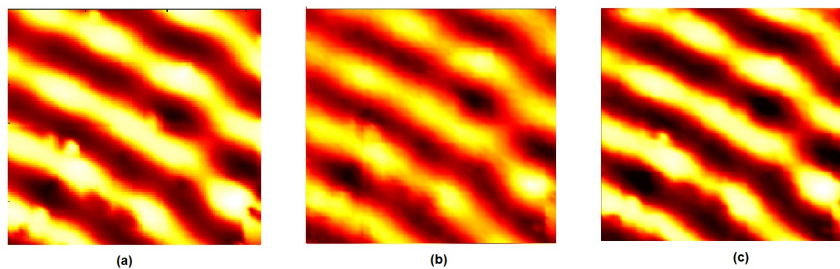




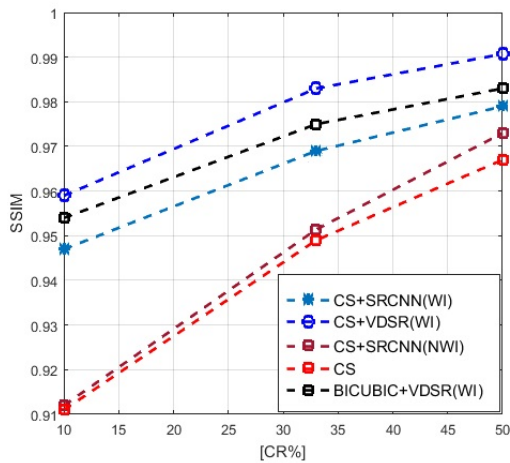
**Figure 8.** Wavefield images recovered for the simple aluminum plate with a clamped mass using various methodologies; (a) The schematic of plate and original wavefield image; (b) images recovered uniquely with the CS procedure for CRs:50%, 33% and 10%; (c) images recovered with the CS and SRCNN; (d) images recovered with the CS and VDSR.



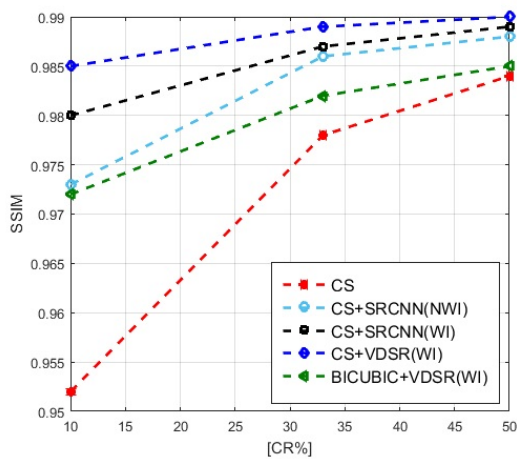
**Figure 9.** (a) HR wavefield image acquired in the simple CFRP plate; (b) CS recovery (CR= 50%); (c) recovered image achieved by combining CS and VDSR.



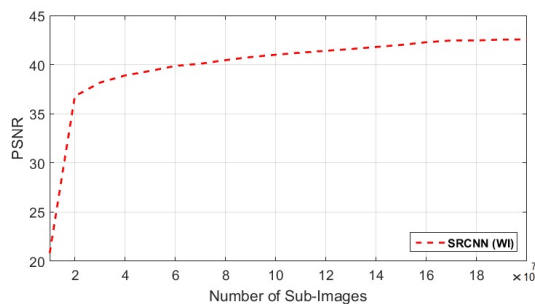
**Figure 10.** (a) HR wavefield image acquired in the simple aluminum plate with a clamped mass; (b) CS recovery (CR= 33%); (c) recovered image achieved by combining CS and VDSR.



**Figure 11.** Comparison of the SSIM between the training models with WI and NWI datasets and the CS technique for an aluminum plate with CR=10%, 33% and 50%.

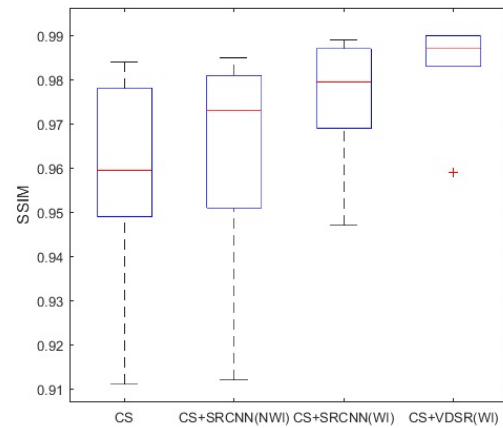


**Figure 12.** Comparison of the SSIM between the training models with WI and NWI datasets and the CS technique for a CFRP plate with CR=10%, 33% and 50%.

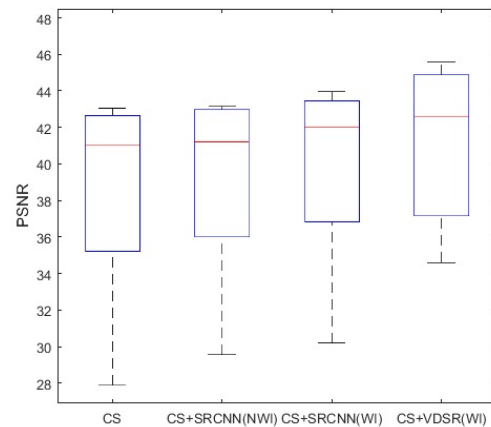


**Figure 13.** Training of SRCNN with the wavefield images (WI) dataset for a curved CFRP plate.

NWI dataset. Table 2 shows that similar trends are obtained by quantifying the effectiveness of the different HR image recovery methods in terms of PSNR. As shown in this Table and in Figs. 11 and 12, the combination of CS and VDSR(WI) demonstrated a performance superior with respect to all the other combinations (including the Bicubic interpolation with VDSR(WI)) in all the considered CRs cases for both plates.



**Figure 14.** Comparison of the SSIM between the CS, the SRCNN scheme, and the VDSR scheme for all the considered cases in the testing dataset with CR=10%, 33% and 50%. In the boxplot representation, the central mark indicates the median, and the bottom and top edges of the box indicate the 25th and 75th percentiles, respectively. The whiskers extend to the most extreme data points.



**Figure 15.** Comparison of the PSNR between the CS, the SRCNN scheme, and the VDSR scheme for all the considered cases in the testing dataset with CR=10%, 33% and 50%. In the boxplot representation, the central mark indicates the median, and the bottom and top edges of the box indicate the 25th and 75th percentiles, respectively. The whiskers extend to the most extreme data points.

To better illustrate the importance of the size of the training dataset in the recovery performance, we have reported in Fig. 13 the PSNR as a function of the dataset cardinality. It can be observed how the cardinality of the dataset improves the performance.

The performance of the different HR image recovery schemes was then quantified on a large testing dataset. As already mentioned, the images used for the evaluation of recovery performances are different from the ones used in the NN training. More specifically, 273 wavefield images, randomly selected among those acquired on the setups shown in Table 1, were used for training, quantitative testing and validation. Such images were down-sampled with different CR ratios.

Figs. 14 and 15 represent the box plot of the SSIM and PSNR in all the considered dataset for: i) CS; ii) SRCNN trained using NWI; iii) SRCNN trained using WI, and VDSR trained using WI. As can be seen, the highest quality HR recovery in terms of SSIM and PSNR is achieved with the VDSR scheme. The mean and the standard error of PSNR of the CS-VDSR (WI) method is 41.21 and 1.65 dB, respectively. This performance is significantly higher than that of the CS-SRCNN (WI) scheme ( $39.75 \pm 2.00$  dB).

From these results, it can be clearly observed that VDSR outperforms SRCNN. This is achieved thanks to the deeper neural network. Besides, residual learning networks, when used in SR tasks, have been proved to possess better visual performance and Peak Signal to Noise Ratio (PSNR) performance<sup>63, 64</sup>. It is also worth nothing that, since deep-learning has recently prospered, many new learning-based algorithms can be used in SISR to replace VDSR, such as VGG<sup>55</sup>, ResNet<sup>65</sup> and GAN<sup>66</sup>.

## Conclusions

HR wavefield scans convey important information about the health status of the inspected structures. However, the acquisition of these images is typically a slow process. For this reason there is a growing interest in finding solutions for speeding up the measurements. One possible solution is based on the reduction of the number of scan points and on the subsequent recovery of the HR image by means of CS procedures. Unfortunately, the quality of this reconstruction method degrades rapidly as the reduction of the scan points becomes more consistent. To counteract this degradation, in this paper, we have investigated the use of SR techniques based on the training of NNs. In particular, we demonstrated two main new findings:

- The training should be performed based on a sufficiently large and comprehensive dataset of wavefield images rather than recurring to conventional image datasets.
- Deep networks have clearly superior performance with respect to shallow neural networks.

Experimental results demonstrate that the proposed methodology can be applied in a variety of structural components to reduce acquisition time and achieve high similarity to the HR images, even when we retain just the 10% of the original scan points.

Future work will investigate: i) The possibility to apply the CS algorithm to raw SLDV data (without averaging); ii) the possibility to exploit this imaging methodology to characterize defects; iii) alternative Deep Learning architectures; iv) the benefit brought by further increasing the number of wavefield images in the training phase with different setups or excitation frequencies. Indeed, it is a well-known fact that deep learning strongly benefits from training on big data. Moreover, the results need to be confirmed in additional cases in order to have a better assessment of the performance, given the vast number of applications which can be targeted by this inspection method.

## Acknowledgements

The authors would like to acknowledge the contribution from the Natural Sciences and Engineering Research Council of Canada (NSERC) and the Consortium for Research and Innovation in Aerospace in Quebec (CRIAQ) for providing the funding for the design and manufacturing of the test structures.

## References

1. Swartz RA, Jung D, Lynch JP et al. Design of a wireless sensor for scalable distributed in-network computation in a structural health monitoring system. In *Proceedings of the 5th International Workshop on Structural Health Monitoring*. pp. 12–14.
2. Mei H, Haider MF, Joseph R et al. Recent advances in piezoelectric wafer active sensors for structural health monitoring applications. *Sensors* 2019; 19(2): 383.
3. Sikdar S and Banerjee S. *Structural Health Monitoring of Advanced Composites Using Guided Waves: Online Monitoring of Defects/Discontinuities in Advanced Composite Structures Using Ultrasonic Guided Waves and PZTs*. LAP LAMBERT Academic Publishing, 2017.
4. Rose JL. A baseline and vision of ultrasonic guided wave inspection potential. *Journal of pressure vessel technology* 2002; 124(3): 273–282.
5. Lowe M and Cawley P. Long range guided wave inspection usage—current commercial capabilities and research directions. *Department of Mechanical Engineering, Imperial College London, London* 2006; : 1–40.
6. Lamb H. On waves in an elastic plate. In *Proceedings of the Royal Society of London A: Mathematical, Physical and Engineering Sciences*, volume 93. The Royal Society, pp. 114–128.
7. Staszewski W, Lee B, Mallet L et al. Structural health monitoring using scanning laser vibrometry: I. lamb wave sensing. *Smart Materials and Structures* 2004; 13(2): 251.
8. Michaels TE, Michaels JE, Thompson DO et al. Application of acoustic wavefield imaging to non-contact ultrasonic inspection of bonded components. In *AIP Conference Proceedings*, volume 820. pp. 1484–1491.
9. Testoni N, De Marchi L and Marzani A. Detection and characterization of delaminations in composite plates via air-coupled probes and warped-domain filtering. *Composite Structures* 2016; 153: 773–781.
10. Di Ianni T, De Marchi L, Perelli A et al. Compressive sensing of full wave field data for structural health monitoring applications. *IEEE transactions on ultrasonics, ferroelectrics, and frequency control* 2015; 62(7): 1373–1383.
11. Esfandabadi YK, De Marchi L, Testoni N et al. Full wavefield analysis and damage imaging through compressive sensing in lamb wave inspections. *IEEE transactions on ultrasonics, ferroelectrics, and frequency control* 2017; 65(2): 269–280.
12. Harley JB and Moura JM. Sparse recovery of the multimodal and dispersive characteristics of Lamb waves. *The Journal of the Acoustical Society of America* 2013; 133(5): 2732–2745.
13. Sabeti S, Leckey CA, De Marchi L et al. Sparse wavenumber recovery and prediction of anisotropic guided waves in composites: A comparative study. *IEEE transactions on ultrasonics, ferroelectrics, and frequency control* 2019; .
14. Alguri KS and Harley JB. Transfer learning of ultrasonic guided waves using autoencoders: A preliminary study. In

- AIP Conference Proceedings*, volume 2102. AIP Publishing, p. 050013.
15. Mesnil O and Ruzzene M. Sparse wavefield reconstruction and source detection using compressed sensing. *Ultrasonics* 2016; 67: 94–104.
  16. Perelli A, Di Ianni T, Marzani A et al. Model-based compressive sensing for damage localization in lamb wave inspection. *IEEE transactions on ultrasonics, ferroelectrics, and frequency control* 2013; 60(10): 2089–2097.
  17. Figueiredo MA, Nowak RD and Wright SJ. Gradient projection for sparse reconstruction: Application to compressed sensing and other inverse problems. *IEEE Journal of selected topics in signal processing* 2007; 1(4): 586–597.
  18. Ma S, Yin W, Zhang Y et al. An efficient algorithm for compressed mr imaging using total variation and wavelets. In *Computer Vision and Pattern Recognition, 2008. CVPR 2008. IEEE Conference on*. IEEE, pp. 1–8.
  19. Krizhevsky A, Sutskever I and Hinton GE. Imagenet classification with deep convolutional neural networks. In *Advances in neural information processing systems*. pp. 1097–1105.
  20. Duan G, Hu W and Wang J. Research on the natural image super-resolution reconstruction algorithm based on compressive perception theory and deep learning model. *Neurocomputing* 2016; 208: 117–126.
  21. Bora A, Jalal A, Price E et al. Compressed sensing using generative models. In *Proceedings of the 34th International Conference on Machine Learning-Volume 70*. JMLR. org, pp. 537–546.
  22. Dong C, Loy CC, He K et al. Image super-resolution using deep convolutional networks. *IEEE transactions on pattern analysis and machine intelligence* 2016; 38(2): 295–307.
  23. Xie J, Xu L and Chen E. Image denoising and inpainting with deep neural networks. In *Advances in neural information processing systems*. pp. 341–349.
  24. Xu L, Ren JS, Liu C et al. Deep convolutional neural network for image deconvolution. In *Advances in Neural Information Processing Systems*. pp. 1790–1798.
  25. Siu WC and Hung KW. Review of image interpolation and super-resolution. In *Signal & Information Processing Association Annual Summit and Conference (APSIPA ASC), 2012 Asia-Pacific*. IEEE, pp. 1–10.
  26. Park B and Sohn H. Reconstruction of laser ultrasonic wavefield images from reduced sparse measurements using compressed sensing aided super-resolution. In *AIP Conference Proceedings*, volume 1806. AIP Publishing, p. 030003.
  27. Schmidhuber J. Deep learning in neural networks: An overview. *Neural networks* 2015; 61: 85–117.
  28. Michaels TE, Michaels JE and Ruzzene M. Frequency-wavenumber domain analysis of guided wavefields. *Ultrasonics* 2011; 51(4): 452–466.
  29. Kudela P, Radziński M and Ostachowicz W. Identification of cracks in thin-walled structures by means of wavenumber filtering. *Mechanical Systems and Signal Processing* 2015; 50: 456–466.
  30. Demanet L and Ying L. Curvelets and wave atoms for mirror-extended images. In *Wavelets XII*, volume 6701. International Society for Optics and Photonics, p. 67010J.
  31. Sohn H, Swenson ED, Olson SE et al. Delamination detection in composite structures using laser vibrometer measurement of lamb waves. In *Health Monitoring of Structural and Biological Systems 2010*, volume 7650. International Society for Optics and Photonics, p. 76500P.
  32. Yu L, Tian Z and Leckey CA. Crack imaging and quantification in aluminum plates with guided wave wavenumber analysis methods. *Ultrasonics* 2015; 62: 203–212.
  33. Park B, An YK and Sohn H. Visualization of hidden delamination and debonding in composites through noncontact laser ultrasonic scanning. *Composites science and technology* 2014; 100: 10–18.
  34. Sohn H, Dutta D, Yang J et al. A wavefield imaging technique for delamination detection in composite structures. Technical report, DTIC Document, 2010.
  35. Owens C, Swenson E and Allen C. Visualization of lamb wave interaction with a 5 mm fatigue crack using 1d ultra high frequency laser doppler vibrometry. Technical report, DTIC Document, 2011.
  36. Migot A, Bhuiyan Y and Giurgiutiu V. Numerical and experimental investigation of damage severity estimation using lamb wave-based imaging methods. *Journal of Intelligent Material Systems and Structures* 2019; 30(4): 618–635.
  37. Kudela P, Radziński M and Ostachowicz W. Impact induced damage assessment by means of lamb wave image processing. *Mechanical Systems and Signal Processing* 2018; 102: 23–36.
  38. Candès EJ, Romberg J and Tao T. Robust uncertainty principles: Exact signal reconstruction from highly incomplete frequency information. *IEEE Transactions on information theory* 2006; 52(2): 489–509.
  39. Hennenfent G and Herrmann FJ. Simply denoise: Wavefield reconstruction via jittered undersampling. *Geophysics* 2008; 73(3): V19–V28.
  40. Candès E and Romberg J. Sparsity and incoherence in compressive sampling. *Inverse problems* 2007; 23(3): 969.
  41. Tropp J and Gilbert AC. Signal recovery from random measurements via orthogonal matching pursuit. *IEEE Transactions on Information Theory* 2005; 53.
  42. Blumensath T and Davies ME. Iterative thresholding for sparse approximations. *Journal of Fourier Analysis and Applications* 2008; 14(5-6): 629–654.
  43. Hale ET, Yin W and Zhang Y. Fixed-point continuation for  $l_1$ -minimization: Methodology and convergence. *SIAM Journal on Optimization* 2008; 19(3): 1107–1130.
  44. Candès EJ and Wakin MB. An introduction to compressive sampling. *IEEE signal processing magazine* 2008; 25(2): 21–30.
  45. van den Berg E, Friedlander M, Hennenfent G et al. Sparco: A testing framework for sparse reconstruction. *Tech Rep TR-2007-20* 2007; .
  46. Park SC, Park MK and Kang MG. Super-resolution image reconstruction: a technical overview. *IEEE signal processing magazine* 2003; 20(3): 21–36.
  47. Glasner D, Bagon S and Irani M. Super-resolution from a single image. In *Computer Vision, 2009 IEEE 12th International Conference on*. IEEE, pp. 349–356.
  48. Li X, Hu Y, Gao X et al. A multi-frame image super-resolution method. *Signal Processing* 2010; 90(2): 405–414.
  49. Keys R. Cubic convolution interpolation for digital image processing. *IEEE transactions on acoustics, speech, and signal processing* 1981; 29(6): 1153–1160.
  50. Freeman WT, Jones TR and Pasztor EC. Example-based super-resolution. *IEEE Computer graphics and Applications* 2002; 22(2): 56–65.

51. Chang H, Yeung DY and Xiong Y. Super-resolution through neighbor embedding. In *Computer Vision and Pattern Recognition, 2004. CVPR 2004. Proceedings of the 2004 IEEE Computer Society Conference on*, volume 1. IEEE, pp. I–I.
52. Aharon M, Elad M, Bruckstein A et al. K-svd: An algorithm for designing overcomplete dictionaries for sparse representation. *IEEE Transactions on signal processing* 2006; 54(11): 4311.
53. LeCun Y, Bengio Y and Hinton G. Deep learning. *nature* 2015; 521(7553): 436.
54. Hinton G, Deng L, Yu D et al. Deep neural networks for acoustic modeling in speech recognition: The shared views of four research groups. *IEEE Signal processing magazine* 2012; 29(6): 82–97.
55. Kim J, Kwon Lee J and Mu Lee K. Accurate image super-resolution using very deep convolutional networks. In *Proceedings of the IEEE conference on computer vision and pattern recognition*. pp. 1646–1654.
56. Simonyan K and Zisserman A. Very deep convolutional networks for large-scale image recognition. *arXiv preprint arXiv:14091556* 2014; .
57. Jia Y, Shelhamer E, Donahue J et al. Caffe: Convolutional architecture for fast feature embedding. In *Proceedings of the 22nd ACM international conference on Multimedia*. ACM, pp. 675–678.
58. Dong C, Loy CC and Tang X. Accelerating the super-resolution convolutional neural network. In *European Conference on Computer Vision*. Springer, pp. 391–407.
59. Yang J, Wright J, Huang TS et al. Image super-resolution via sparse representation. *IEEE transactions on image processing* 2010; 19(11): 2861–2873.
60. Deng J, Dong W, Socher R et al. Imagenet: A large-scale hierarchical image database. In *Computer Vision and Pattern Recognition, 2009. CVPR 2009. IEEE Conference on*. Ieee, pp. 248–255.
61. Huynh-Thu Q and Ghanbari M. Scope of validity of psnr in image/video quality assessment. *Electronics letters* 2008; 44(13): 800–801.
62. Wang Z, Bovik AC, Sheikh HR et al. Image quality assessment: from error visibility to structural similarity. *IEEE transactions on image processing* 2004; 13(4): 600–612.
63. Wang Z, Chen J and Hoi SC. Deep learning for image super-resolution: A survey. *arXiv preprint* 2019; : 1–23.
64. Yang W, Zhang X, Tian Y et al. Deep learning for single image super-resolution: A brief review. *IEEE Transactions on Multimedia* 2019; : 1–16.
65. Li D and Wang Z. Video superresolution via motion compensation and deep residual learning. *IEEE Transactions on Computational Imaging* 2017; 3(4): 749–762.
66. Ledig C, Theis L, Huszár F et al. Photo-realistic single image super-resolution using a generative adversarial network. In *Proceedings of the IEEE conference on computer vision and pattern recognition*. pp. 4681–4690.